INTERNATIONAL JOURNAL FOR NUMERICAL METHODS IN FLUIDS, VOL. 20, 603–620 (1995)

TIME-DEPENDENT LIQUID METAL FLOWS WITH FREE CONVECTION AND A DEFORMABLE FREE SURFACE

MATTHEW A. McCLELLAND

Lawrence Livermore National Laboratory, Livermore, CA 94550, U.S.A.

SUMMARY

The finite element method is employed to investigate time-dependent liquid metal flows with free convection, free surfaces and Marangoni effects. The liquid circulates in a two-dimensional shallow trough with differentially heated vertical walls. The spatial formulation incorporates mixed Lagrangian approximations to the velocity, pressure, temperature and free surface position. The time integration is performed with the backward Euler and trapezoid rule methods with step size control. The Galerkin method is used to reduce the problem to a set of non-linear equations which are solved with the Newton–Raphson method. Calculations are performed for conditions relevant to the electron beam vaporization of refractory metals. The Prandtl number is 0·015 and Grashof number are in the transition range between laminar and turbulent flow. The results reveal the effects of flow intensity, surface tension gradients, mesh refinement and time integration strategy.

KEY WORDS free surface; free convection; time-dependent flow; metal flow; finite element method

1. INTRODUCTION

Time-dependent liquid metal flows are important in a wide variety of industrial applications. One process of interest is the electron beam vaporization of refractory metals. In this process an electron beam is used to heat metal confined in a crucible with a cooled wall (see Figure 1). A fraction of the energy is used to vaporize the metal, while the balance skips to a beam dump, radiates to the surroundings and conducts to the crucible wall. A liquid pool forms in the region where the beam strikes and it circulates as a result of buoyancy and capillary forces. The flow is always time-dependent, located in the transition region between laminar and turbulent flow. At high vaporization rates a depression or 'trench' forms from the thrust of the departing vapour. Transport phenomena in the trench and pool strongly influence the vaporization rate and vapour properties. Other features of this process along with factors relating to design and implementation are discussed by Hill.[1]

Time-dependent liquid metal flows are also encountered in crystal growth, welding and metal-casting systems. In crystal growth, convective flow transitions from steady laminar to periodic and chaotic flows can significantly alter the solidification and final microstructure of the crystal. For welding operations the flow characteristics of the liquid metal pool affect the shape and quality of the weld. Flow patterns in metal moulds play a role in the end-use properties of the cast product.

In all the above systems the transport of mass, momentum and energy is coupled with moving phase boundaries. In addition, system behaviour can be influenced by thermal radiation and interaction with vapour or gases. The transport phenomena in these systems have been investigated to varying degrees.

CCC 0271–2091/95/070603–18

Received 7 April 1992
Revised 25 October 1993

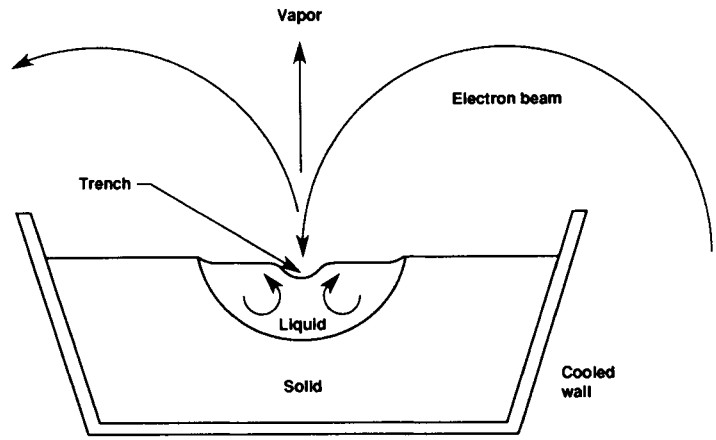

Figure 1. Electron beam vaporizer for metals

Several literature reviews are available for crystal growth systems.[2–5] The results of more recent investigations involving computer modelling were presented at a NATO workshop.[6] Studies of weld pool systems have been made by Tsai and Kou,[7] Zacharia *et al.*[8] and Choo and Szekely.[9] Recent investigations of transport phenomena in metal casting have been made by Mishima and Szekely,[10] Dhatt *et al.*[11] and Song *et al.*[12] For electron beam vaporization an analysis of flow and heat transfer was made by Kheshgi and Gresho.[13]

Most computational approaches have been directed towards flow with rigid liquid–gas interfaces, while relatively few have treated deformable interfaces. Transient liquid metal flows in rigid domains were simulated in early studies by Jones[14] and Benocci.[15] Gresho and Upson[16] analysed free convection in a square cavity and Mohamad and Viskanta[17] extended these results to determine critical values for the Grashof number and frequency at the onset of oscillatory flow. A number of investigators[3,18–22] have calculated time-dependent, two- and three- imensional flows in idealized crystal growth systems consisting of rigid cylinders.

Attention has also focused on buoyancy-driven flows in shallow two-dimensional cavities with vertical walls maintained at different temperatures. Crochet *et al.*[23,24] applied finite difference and finite element methods to obtain steady state and time-dependent solutions. Winters[25] used a perturbation method with finite elements to determine critical conditions for the onset of oscillations. In a GAMM workshop[26,27] the performance of numerical methods was compared for flows in the vicinity of this transition point. With sufficient resolution in space and time, there was good agreement for such variables as the critical Grashof number and frequency.

Steady state liquid metal flows with deformable free surfaces have been investigated in a few studies. Brown and co-workers[28,29] used the finite element method to analyse Czochralski crystal growth systems with deformable liquid–gas and liquid–solid interfaces joined at a tri-junction. Tsai and Kou[7] employed the SIMPLE algorithm with deforming orthogonal curvilinear co-ordinates to treat the liquid–gas interface in a weld pool. In their analysis the solid–liquid interface was handled using a mushy zone.

Temperature-induced Marangoni effects were also included in two of these steady state analyses involving deformable free surfaces. In the analysis of Czochralski crystal growth[28] the Marangoni effect greatly accelerated the flow, forming a thin boundary layer and significantly changing the shape of the free surface. In the absence of buoyancy forces, changing the sign of the Marangoni effect significantly changed the shape of the weld pool.[7]

For liquid metal flows in rigid containers, Marangoni effects have been incorporated in many steady state simulations but far fewer time-dependent calculations. Ben Hadid and Roux[30] calculated results for flow in a rigid rectangular cavity under conditions near the transition point between steady state and oscillatory flow. They found that the Marangoni effects tends to stabilize the flow for both positive and negative contributions, except for a narrow negative range. Villers and Platten[31] give results for the same flow system that also show stabilization for positive contributions of the Marangoni effect.

In this study we investigate the flow in a shallow two-dimensional trough with differentially heated side walls (see Figure 2). Temperature-induced Marangoni effects are included at the deformable top free surface. This surface is treated numerically using the methods developed by Kistler and Scriven[32] for steady state coating flows. A similar approach was employed by Brown *et al.*[28] and Sackinger *et al.*[29] in the finite element analysis of Czochralski crystal growth. The time integration is performed with the trapezoid rule developed by Gresho *et al.*[33] and applied to free surface flows by Kheshgi and Scriven.[34] Results are obtained for flow intensities as large as those observed in e-beam vaporizer pools and they reveal the effects of mesh and time step refinement.

2. BASIC EQUATIONS

2.1. *Equations of change*

We investigate a Newtonian liquid that has constant bulk properties, except for the density which varies linearly with temperature according to the Boussinesq approximation. The scaled mass, momentum and energy equations are

$$\nabla \cdot \mathbf{v} = 0, \tag{1}$$

$$Gr^{1/2}\left(\frac{\partial \mathbf{v}}{\partial t} + \mathbf{v} \cdot \nabla \mathbf{v}\right) = -\nabla \cdot \boldsymbol{\pi} + \left(\frac{1}{St} - Gr^{1/2}T\right)\boldsymbol{\delta}_g, \tag{2}$$

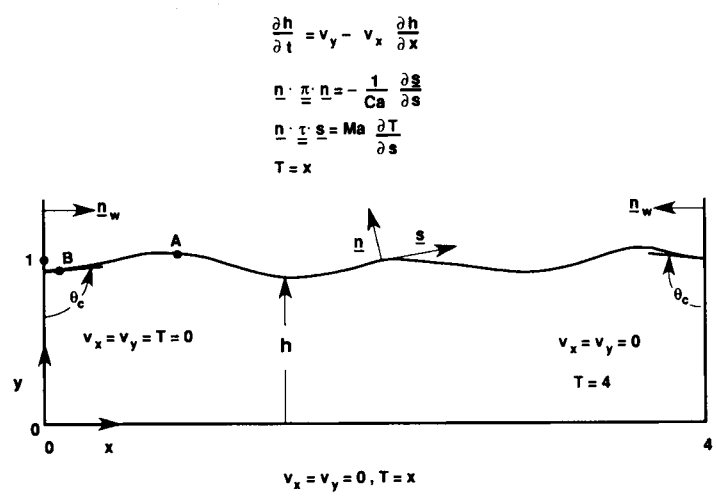

Figure 2. Co-ordinates and boundary conditions for flow in a rectangular trough. Point A is located at $x = 0{\cdot}8$ and $y = h$. Point B is located at $x = 0{\cdot}08$ and $y = h$

$$Gr^{1/2}Pr\left(\frac{\partial T}{\partial t}+\mathbf{v}\cdot\nabla T\right)=-\nabla\cdot\mathbf{q}. \tag{3}$$

The total stress tensor $\boldsymbol{\pi}$ and heat flux vector q are given by

$$\boldsymbol{\pi}=p\boldsymbol{\delta}-\left[\nabla\mathbf{v}+(\nabla\mathbf{v})^{\dagger}\right], \tag{4}$$

$$\mathbf{q}=-\nabla T. \tag{5}$$

The scaled variables are given by

$$\begin{aligned} &t=t^{+}v_s/h_s, \qquad \mathbf{x}=\mathbf{x}^{+}/h_s, \qquad \mathbf{v}=\mathbf{v}^{+}/v_s,\\ &\boldsymbol{\pi}=\boldsymbol{\pi}^{+}h_s/\mu_0 v_s, \qquad p=p^{+}h_s/\mu_0 v_s,\\ &T=(T^{+}-T_0)L/h_s(T_1-T_0), \qquad \mathbf{q}=\mathbf{q}^{+}L/[k_0(T_1-T_0)], \end{aligned} \tag{6}$$

in which 'pluses' denote dimensional variables. Here L is the length of the trough and h_s is a characteristic depth of the liquid, which is taken to be $L/4$ for the cases described below. Also, T_0 and T_1 are the dimensional temperatures at the boundaries $x=0$ and $x=4$ respectively. The properties μ_0 and k_0 are the viscosity and thermal conductivity evaluated at T_0. A velocity standard is obtained from a characteristic balance of buoyancy and inertial forces:

$$v_s=\left[\beta(T_1-T_0)gh_s^2/L\right]^{1/2}. \tag{7}$$

Here β is the volumetric thermal expansion coefficient. The dimensionless groups are

$$Gr=\frac{\beta(T_1-T_0)gh_s^4}{v_0^2L}, \qquad Pr=\frac{v_0}{\alpha_0}, \qquad St=\left(\frac{\beta(T_1-T_0)v_0^2}{gh_s^2L}\right)^{1/2}, \tag{8}$$

in which v_0 and α_0 are kinematic viscosity and thermal diffusivity evaluated at T_0. Note that the Reynolds, Peclet and Rayleigh numbers are related to the Grashof and Prandtl numbers by $Re=Gr^{1/2}$, $Pe=Gr^{1/2}\,Pr$ and $Ra=GrPr$.

2.2. *Boundary and initial conditions*

The problem statement given by equations (1)–(3) is completed with the specification of boundary and initial conditions for the free convection system of Figure 2. The kinematic condition is the statement that no liquid penetrates the liquid–gas interface:

$$\mathbf{n}\cdot\frac{\partial\mathbf{X}}{\partial t}=\mathbf{n}\cdot\mathbf{v} \quad \text{at } \mathbf{x}=\mathbf{X}. \tag{9}$$

Here $\mathbf{X}$ and $\mathbf{n}$ are the respective position and normal vectors for the liquid–gas interface. For the trough of Figure 2, equation (9) takes the form

$$\frac{\partial h}{\partial t}=v_y-v_x\frac{\partial h}{\partial x} \quad \text{at } y=h, \tag{10}$$

in which v_x and v_y are components of the velocity vector.

For steady state calculations an additional boundary condition must be specified for the variable h. One possibility is to set the total mass of liquid in the trough. In order to use this condition, the numerical solution method described in the next section would have to be modified to treat partially banded matrices.[35,36] Instead we use

$$h=1 \quad \text{at } x=4, \tag{11}$$

which is more easily implemented and provides similar results. For transient cases the contact line is able to move and equation (11) is not applied.

At the free surface between the liquid and gas, which is to a good approximation inviscid and inertialess, a force balance gives[37]

$$\mathbf{n} \cdot \boldsymbol{\pi} = -\frac{\sigma/\sigma_0}{Ca}\frac{\partial s}{\partial s} - \frac{s}{Ca}\frac{\partial(\sigma/\sigma_0)}{\partial s}, \tag{12}$$

in which s is the unit tangent vector, s is the distance measured along the interface in the direction s and $\partial s/\partial s$ is the curvature of the interface (see Figure 2). Also, σ is the surface tension and the capillary number is given by

$$Ca = \frac{\mu_0 v_s}{\sigma_0}. \tag{13}$$

In the development of equation (12) the ambient gas pressure is taken to be negligible. The first term on the right-hand side is the normal component resulting from surface curvature. The second term is the tangential component resulting from gradients in the surface tension. If the surface tension is a linear function of temperature, equation (12) becomes

$$\mathbf{n} \cdot \boldsymbol{\pi} = -\frac{1}{Ca}\frac{\partial \mathbf{s}}{\partial s} + Ma\frac{\partial T}{\partial s}\mathbf{s}. \tag{14}$$

For the normal component the effects of surface tension gradients are assumed to be of lesser importance ($\sigma/\sigma_0 \approx 1$). In the tangential component the Marangoni number is a characteristic ratio of surface tension gradient forces to viscous forces:

$$Ma = -\frac{1}{\mu_0}\frac{\mathrm{d}\sigma}{\mathrm{d}T}\left(\frac{T_1 - T_0}{L\beta g}\right)^{1/2}. \tag{15}$$

Note that this definition, which is of the form $Ma = (-\mathrm{d}\sigma/\mathrm{d}T)\Delta T/\mu v_s$, differs from two other more commonly used definitions: $Ma_v = (-\mathrm{d}\sigma/\mathrm{d}T)L_s\Delta T/\rho v^2$ and $Ma_\alpha = (-\mathrm{d}\sigma/\mathrm{d}T)L_s\Delta T/\rho v\alpha$. Here ΔT and L_s are standards for the temperature difference and length scale respectively.

For steady state cases a contact angle θ_c is specified at each of the two static contact lines where liquid interfaces intersect the solid walls (see Figure 2):

$$\mathbf{n}_w \cdot \mathbf{n} = \cos\,\theta_c \quad \text{at } x = 0 \text{ and } y = h, \tag{16}$$

$$\mathbf{n}_w \cdot \mathbf{n} = \cos\,\theta_c \quad \text{at } x = 4 \text{ and } y = h. \tag{17}$$

Here n_W is the inward-pointing normal vector for the trough wall. For time-dependent cases the contact line moves and there is less certainty in the choice of boundary conditions.[32] For these cases we also use equations (16) and (17) and employ θ_c as an apparent dynamic contact angle. The no-slip condition is employed at the three solid boundaries, which is valid except near moving contact lines (see Figure 2). At these lines there is an apparent stress singularity which can be treated by introducing a slip condition of some type.[32] Possibilities include a specified slip velocity, slip by discretization and Navier's mixed condition. In this work the no-slip condition is applied at all solid boundaries and slip by discretization is used. Navier's mixed boundary condition is physically more reasonable but involves the use of a slip coefficient. The thermal boundary conditions are specified temperatures at each of the boundaries. Different temperatures are maintained at each of the vertical walls and linearly interpolated temperatures are used at the other two boundaries. For time-dependent cases the problem statement is completed with the specification of an initial condition which is a steady state solution at a lower Grashof number.

3. NUMERICAL METHOD

3.1. Spatial discretization

The equations of change (1)–(3) and associated boundary conditions are discretized in space using a mixed finite element basis set and Galerkin method. The velocity, pressure and temperature are represented by Lagrangian linear and quadratic polynomials:

$$\begin{aligned} \mathbf{v} &= \sum_{i=1}^{N} \left(v_x^i \delta_x + v_y^i \boldsymbol{\delta}_y \right) \Phi^i(x, y), & T &= \sum_{i=1}^{N} T^i \Phi^i(x, y), \\ p &= \sum_{j=1}^{N_p} p^j \Gamma^j(x, y), & h &= \sum_{k=1}^{N_h} h^k \Phi^k(x, h). \end{aligned} \tag{18}$$

We employ nine-node biquadratic polynomials Φ^i for the velocity and temperature, four-node bilinear polynomials $\Gamma^i(x, y)$ for the pressure and three-node quadratic polynomials $\Phi^k(x, h)$ for the pool depth. The total number of nodes is denoted by N, while N_p and N_h are the number of pressure and surfaces nodes respectively. It is noted that this representation of the field variables is generally satisfactory. However, in the case of strong convection and marginal spatial resolution, superior performance could be achieved with linear polynomials for v, T and h and a piecewise constant pressure[33] or penalty formulation for the pressure.[38] Other possibilities include quadratic representations of v, T and h combined with discontinuous linear interpolation of the pressure to yield element level mass balances.[29,33]

The Cartesian co-ordinates (x, y) are related to local elemental co-ordinates (ξ, η) through a Lagrangian isoparametric mapping:

$$x = \sum_{I=1}^{9} x^I \phi^I(\xi, \eta), \qquad y = \sum_{I=1}^{9} y^I \phi^I(\xi, \eta). \tag{19}$$

For the flow of Figure 2 the grid is 'stretched' linearly in the y-direction as the free surface moves. The motion of an interior node is given by

$$y^i = h(x^i) y_0^i / h_0(x^i), \tag{20}$$

in which the subscript '0' denotes a quantity for the unstretched mesh.

For the conversion of the equations of change (1)–(3) into Galerkin residual expressions, the time derivatives in fixed co-ordinates are written in terms of quantities that move with the mesh:[34]

$$\frac{\partial \mathbf{v}}{\partial t} = \left.\frac{\partial \mathbf{v}}{\partial t}\right|_{\mathrm{m}} - \dot{\mathbf{x}}_{\mathrm{m}} \cdot \nabla \mathbf{v}, \qquad \frac{\partial T}{\partial t} = \left.\frac{\partial T}{\partial t}\right|_{\mathrm{m}} - \dot{\mathbf{x}}_{\mathrm{m}} \cdot \nabla T. \tag{21}$$

Here $\dot{\mathbf{x}}_{\mathrm{m}}$ is the velocity of a point which moves with the mesh:

$$\dot{\mathbf{x}}_{\mathrm{m}} = \frac{\partial \mathbf{x}_{\mathrm{m}}}{\partial h} \frac{\partial h}{\partial t} = \frac{y_0}{h_0} \frac{\partial h}{\partial t} \delta_y. \tag{22}$$

The residual expressions are formed for the equations of change (1)–(3). The continuity equation is

$$R_c \equiv \int_A \Gamma^j \nabla \cdot \mathbf{v}\, dA = 0, \tag{23}$$

in which $j = 1, .608.608.608, N_p$. The residual expressions formed from the momentum and energy equations are written in the weak form. In this transformation the stress and heat flux terms are integrated by parts. In terms of variables that move with the mesh (dropping the subscript 'm'), the residuals for the momentum and energy equations are

$$\mathbf{R}_M \equiv \int_A \left[\Phi^i (Gr)^{1/2}\left(\frac{\partial \mathbf{v}}{\partial t} + (\mathbf{v} - \dot{\mathbf{x}}) \cdot \nabla \mathbf{v}\right) - \Phi^i \delta_g \left(\frac{1}{St} - (Gr)^{1/2} T\right)\right] dA$$

$$- \int_A \nabla \Phi^i \cdot \boldsymbol{\pi}\, dA + \int_s \Phi^i \mathbf{n} \cdot \boldsymbol{\pi}\, ds = 0, \tag{24}$$

$$R_E \equiv \int_A \left[\Phi^i (Gr)^{1/2} Pr\left(\frac{\partial T}{\partial t} + (\mathbf{v} - \dot{\mathbf{x}}) \cdot \nabla T\right) - \nabla \Phi^i \cdot \mathbf{q}\right] dA + \int_s \Phi^i \mathbf{n} \cdot \mathbf{q}\, ds = 0, \tag{25}$$

in which $i = 1, .608.608.608, N$ represents the residual equation for each node.

The residuals for the kinematic boundary condition (9) are given by

$$R_K \equiv \int_s \Phi^k(x, h)\left(\mathbf{n} \cdot \frac{\partial \mathbf{X}}{\partial t} - \mathbf{v} \cdot \mathbf{n}\right) ds, \tag{26}$$

with $k = 1, .608.608.608, N_h$. The free surface boundary term for the momentum residual is evaluated with the use of equation (14). The term involving Ca is integrated by parts to eliminate the surface curvature $\partial \mathbf{s}/\partial s$ in favour of the unit tangent s:[39]

$$\int_s \Phi^i \mathbf{n} \cdot \boldsymbol{\pi}\, ds = -\frac{1}{Ca}\Phi^i(s_1 - s_0) + \frac{1}{Ca}\int_s \mathbf{s} \cdot \frac{\partial \Phi^i}{\partial s}\, ds + Ma \int_s \Phi^i \mathbf{s} \frac{\partial T}{\partial s}\, ds. \tag{27}$$

Here s_0 and s_1 are the unit tangent vectors along the free surface evaluated at $x = 0$ and $x = 4$ respectively. However, at contact lines the no-slip condition is applied and equations (24) and (27) are not used as written. The contact angle conditions (16) and (17) are imposed in their natural form by replacing the kinematic residuals (26) by[32]

$$\mathbf{n}_\theta \cdot \mathbf{R}_M = 0 \quad \text{at } x = 0 \text{ and } y = h, \tag{28}$$

$$\mathbf{n}_\theta \cdot \mathbf{R}_M = 0 \quad \text{at } x = 4 \text{ and } y = h, \tag{29}$$

Here n_θ is the vector n that satisfies equation (16) or (17). The momentum residual (24) includes equation (27) without the terms involving s_0 and s_1. In the absence of the kinematic conditions the contact lines are able to move even though no-slip conditions are applied at all locations along the walls. This is the method of slip by discretization mentioned above. Finally, for steady state cases the surface boundary condition (11) is applied as an essential condition in place of the continuity residual (23) at the location $(x = 4, y = 0)$. This has the same effect as adjusting a nodal pressure to set the fluid level in the trough.

The boundary conditions described above are shown in Figure 3 for a two-element mesh. Except for the pressure condition at node 9, all conditions apply to both steady state and transient cases.

For the cases described below, three meshes of differing refinement are used which are symmetric

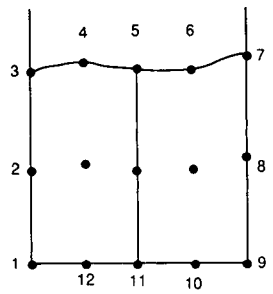

nodes	ss/t	Variables v	p	T	h
1, 11	ss, t	e	c	e	—
2, 8, 10, 12	ss, t	e	—	e	—
3, 7	ss, t	e	c	e	θ
4, 6	ss, t	s	—	e	k
5	ss, t	s	c	e	k
9	ss	e	h	e	—
9	t	e	c	e	—

Figure 3.–Variables and conditions for boundary nodes in a two-element mesh: θ, contact angle condition (28) or (29); c, continuity equation (23); k, kinematic condition (26); h, height condition (11); e, essential condition; ss, steady state case; s, surface condition (27); t, time-dependent case

about the lines $x=2$ and $y=0{\cdot}5$ (see Figure 4). For the unstretched mesh ($h=1$), element boundary locations in the quadrant ($0<x<2$, $0<y<0{\cdot}5$) are given by

$$x_0^i = 2\frac{1-\exp(2i/n_{e,x})}{1-\exp(1)}, \quad i = 1, 2, \ldots, n_{e,x}/2,$$
$$y_0^i = \frac{1}{2}\frac{1-\exp(2i/n_{e,y})}{1-\exp(1)}, \quad i = 1, 2, \ldots, n_{e,y}/2, \tag{30}$$

in which $n_{e,609x}$ and $n_{e,609y}$ are the numbers of elements in the x- and y-directions.

3.2. *Time integration method*

The discretized equations of change (23)–(26) are integrated in time using the trapezoid rule (TR) and backward Euler (BE) methods with automatic error control.[33,40] For each of these methods a local integration error e is calculated at each time step based on the difference between a predicted solution Z_p given by an explicit method and a corrected solution Z_c calculated by an implicit method. The square-root norms for the two methods are given by

$$e_{BE} = \left\| \frac{\mathbf{Z}_{n+1}^{p} - \mathbf{Z}_{n+1}^{c}}{2 + \Delta t_{n-1}/\Delta t_n} \right\|_2, \tag{31}$$

$$e_{TR} = \left\| \frac{\mathbf{Z}_{n+1}^{p} - \mathbf{Z}_{n+1}^{c}}{3(1 + \Delta t_{n-1}/\Delta t_n)} \right\|_2. \tag{32}$$

The time step is adjusted for the next step based on a comparison between this error and a user-specified tolerance ε. In this work we generally use $\varepsilon = 1 \times 10^{-3}$, except in a few cases for which we employ $\varepsilon = 1 \times 10^{-4}$ to examine the effects of time step refinement.

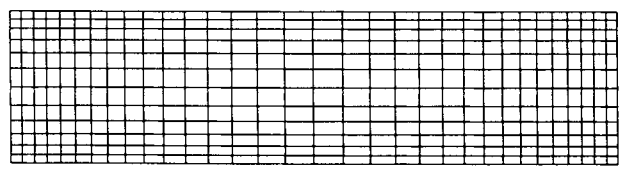

Figure 4. Unstretched 32 × 12 finite element meshes for natural convection in a rectangular trough (5369 unknowns). Element locations are given by equation (30). Meshes not shown: 48 × 18, 11,795 unknowns; 64 × 24, 20,717 unknowns

The non-linear algebraic equations are solved for v, p, T and h using the Newton–Raphson method, which linearizes the equations. The development and assembly of equations follow the approach employed by Kistler and Scriven[32] and extended for transient problems by Kheshgi and Scriven.[34] The linear equation set is solved at each iteration or time step by Gaussian elimination. A modified frontal solver is employed which is based on the one given by Hood.[41] For the 64×24 mesh a single time step required 0·9 h of CPU time on a DECstation 3100.

The TR method is used in most cases since it is more accurate and non-dissipative. The BE method is used as a starting method for the TR method. It is also employed during the initial stages of calculations to damp spurious oscillations resulting from sudden changes in conditions.

4. RESULTS

Steady state and time-dependent solutions are presented for the natural convection system of Figure 2. The length of the trough is varied while the aspect ratio L/h_s is held constant at 4. A constant temperature difference $T_1 - T_0 = 1000$ °C is applied which is representative for the electron beam vaporization of refractory metals. A model refractory metal is investigated which has the following properties:

$$\rho_0 = 1 \times 10^4 \text{ kg m}^{-3}, \quad \mu_0 = 3 \times 10^{-3} \text{ kg m}^{-1} \text{ s}^{-1}, \quad \beta = 1 \times 10^{-4} \text{ °C}^{-1},$$
$$\alpha_0 = 2 \times 10^{-5} \text{ m}^2 \text{ s}^{-1}, \quad \sigma_0 = 1.25 \text{ N m}^{-1}, \quad -1.5 \times 10^{-4} \text{ N m}^{-1} \text{ °C}^{-1} \leq d\sigma/dT \leq 0.$$

A range of values for $d\sigma/dT$ is considered given the variations which may result from surface contamination.[42] The contact angle is taken to be $\theta_c = 90°$. For these properties and flow conditions the dimensionless groups of equations (8), (13) and (15) are written as functions of Gr:

$$St = 0.025 Gr^{-1/2}, \quad Pr = 0.015, \quad Ca = 1 \times 10^{-5} Gr^{1/6}, \quad 0 \leq Ma \leq 3 \times 10^3 Gr^{-1/6}. \tag{33}$$

The Grashof number is varied from 1×10^4 to 1×10^6, which overlaps the range $1 \times 10^5 \leq Gr \leq 1 \times 10^8$ for electron beam vaporization of metals. The above value for Pr was used in previous investigations.[23–26] The respective increase and decrease in Ca and Ma with Gr reveal that the relative importance of capillary effects decreases with trough size.

4.1. Tests results for flow in a rigid cavity

In order to test the performance of the numerical scheme, a number of calculations were obtained for flow in a rigid cavity with $h = 1$. For $Gr = 1 \times 10^4$, $Ma = 0$ and steady state conditions a value for $|\psi|_{max}$ is compared with a reference solution calculated by Behnia and de Vahl Davis.[43] The value for the 64×24 mesh agrees exactly with the reference value of 0·5529 to the indicated accuracy.

Transient calculations were performed for $Gr = 1 \times 10^4$ and $Ma = 0$ using the 32×12 mesh with the TR method and $\varepsilon = 1 \times 10^{-4}$. This value of Gr is close to the value of $1{\cdot}49 \times 10^4$ calculated by Winters[25] for the onset of oscillatory flow. The calculated frequency of 0·663 compares quite well with the value of 0·664 obtained by Winters. Additional comparisons are given elsewhere.[44]

4.2. Steady state results with a deformable free surface

Steady state streamlines and temperature contours are shown in Figure 5 for the 64×24 mesh with $Gr = 1 \times 10^5$ and 1×10^6 and $Ma = 0$ and 160. For the cases with $Ma = 0$ there are three cells with counterclockwise circulation, while there is only one cell with strong circulation for $Ma = 160$. In the latter case, flow velocities are high in this cell and near the free surface but relatively low elsewhere. For all cases, the curvature of the isotherms reveals that the contribution of thermal convection is

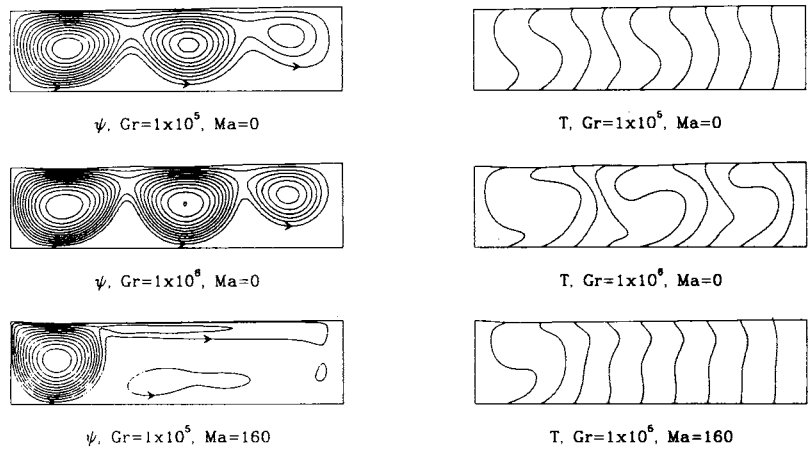

Figure 5. Steady state streamlines and temperature contours for the 64 × 24 mesh. *St*, *Ca* and *Pr* are given by equation (33). Twelve equal increments in ψ for $\psi_{min} \leq \psi \leq \psi_{max}$. Ten equal increments in T for $0 \leq T \leq 4$. The streamlines are calculated using the procedure of Appendix I

moderate. The free surfaces are nearly horizontal, indicating large gravitational and surface tension components. Slight depressions are visible near regions where the streamlines are closely spaced. This suggests some type of Bernoulli effect in which a high velocity is associated with a low pressure and a depression in the free surface.

The smooth streamlines and temperature suggest that the spatial resolution provided by the 64 × 24 mesh is adequate. A mesh refinement study[45] reveals small differences in a surface velocity component $v_{x,611A}$ for $Gr = 1 \times 10^5$. In the case with $Gr = 1 \times 10^6$ a converged solution was found for the 64 × 24 mesh alone. In principle, steady state solutions can be calculated at larger values of *Gr* and *Ma* with additional mesh refinement.[25] However, it is likely that the above steady state solutions are unstable to small disturbances. Although not done here, the stability of each steady state solution could be established by performing a time-dependent simulation. For time variations of constant or increasing amplitude the steady state solution is unstable.

4.3. Time-dependent results for $Gr = 1 \times 10^6$ and $Ma = 0$

Time-dependent calculations were performed for $Gr = 1 \times 10^6$ and $Ma = 0$ with the other dimensionless groups given by equation (33). The initial condition is a steady state, creeping flow

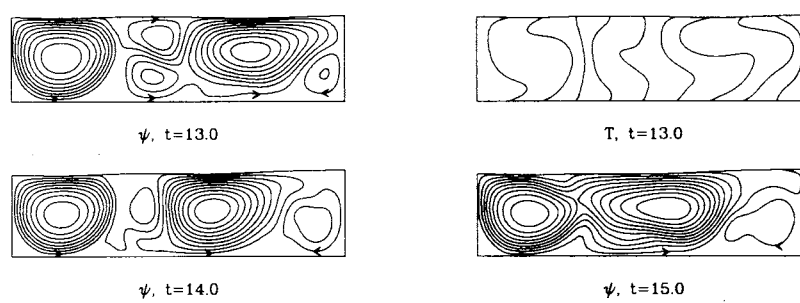

Figure 6. Time-dependent streamlines and temperature contours for $Gr = 1 \times 10^6$, $Ma = 0$, $Ca = 1 \times 10^{-4}$, $St = 2{\cdot}5 \times 10^{-5}$, $Pr = 0{\cdot}015$, 64 × 24 mesh, with TR and $\varepsilon = 1 \times 10^{-3}$. Twelve equal increments in ψ for $\psi_{min} \leq \psi \leq \psi_{max}$. Ten equal increments in T for $0 \leq T \leq 4$

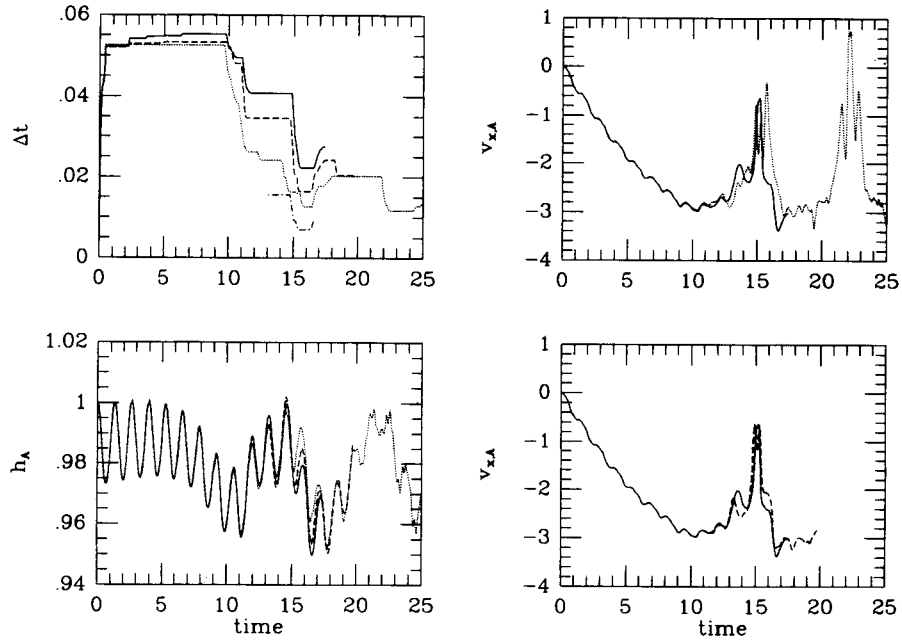

Figure 7.–Time step size and pool depth at location A versus time for $Gr = 1 \times 10^6$, $Ma = 0$, $Ca = 1 \times 10^{-4}$, $St = 2{\cdot}5 \times 10^{-5}$ and $Pr = 0{\cdot}015$. Note that h_A and $v_{x,613A}$ curves for 48×18 mesh coincide.————, 64×24 TR, $\varepsilon = 1 \times 10^{-3}$;— — —, 48×18, TR, $\varepsilon = 1 \times 10^{-3}$;· · · ·, 32×12, TR, $\varepsilon = 1 \times 10^{-3}$; –·–·–, 48×18, TR, $\varepsilon = 1 \times 10^{-4}$

solution. All dimensionless groups for this initial condition are the same as those for the simulation, except for Gr which has the value of 1×10^{-4}. A sequence of streamfunction and temperature contours is shown in Figure 6 for the 64×24 mesh. The flow and temperature fields are well resolved, since the contours are smooth. The flow is quite complex, with at least three cells present at any instant in time. As time progresses, two large cells with rapid counterclockwise circulation merge.

The effects of mesh and time step refinement are shown in evolutionary plots of Δt, h_A, and $v_{x,612A}$ (see Figure 7). Results for four cases are shown in which three meshes and ε-values of 1×10^{-3} and 1×10^{-4} are used. Given the large amount of computing time required to reach a quasi-steady state, the case with $\varepsilon = 1 \times 10^{-4}$ and the 48×18 mesh was started at $t = 13{\cdot}0$ and concluded at $t = 16{\cdot}6$. The solution for the 48×18 mesh and $\varepsilon = 1 \times 10^{-3}$ was used as an initial condition at $t = 13$.

In the flow development period ($0 \leq t \leq 10$) the flow intensity is relatively small and values for Δt are large (see Figure 7). The initial disturbance generates oscillations in h_A with a frequency of approximately 0·75. The velocity $v_{x,612A}$ increases in magnitude and oscillates with nearly the same frequency. The effects of mesh refinement are small for this interval.

It is of interest to compare the frequency of oscillation for gravity-driven surface waves in a two-dimensional, 4×1 trough. For these waves Lamb[46] gives the dimensional frequency for the primary mode as

$$f^+ = \left(\frac{g}{4\pi L \coth(\pi h_s / L)} \right)^{1/2}. \tag{34}$$

This expression is rewritten in terms of the dimensionless variables and groups of equations (6) and (8) as

$$f = \left(\frac{h_s}{4\pi L Gr^{1/2} St \coth(\pi h_s / L)} \right)^{1/2}. \tag{35}$$

Insertion of the case expressions (33) gives the following frequency which does not depend on Gr:

$$f613 = 0{\cdot}722.$$

This result compares fairly well with the value of 0·75 given above, which suggests that the initial oscillations of Figure 7 are driven primarily by gravity.

For $t > 10$ the flow intensity increases and values for Δt are much smaller (see Figure 7). The gravity-driven oscillations are still evident in the curves for h_A. Also present are components of higher and lower frequency. The lower-frequency variations are associated with the global rearrangement of cells (see Figure 6). Higher-frequency fluctuations are present for $t > 20$. However, the results for this interval were only calculated with the 32×12 mesh and would have to be verified by extending the results for the finer meshes. The velocity $v_{x,613A}$ exhibits large variations as the arrangement of cells changes (see Figures 6 and 7). In addition, the regular pattern of oscillation observed in the flow development period ($0 \leq t \leq 10$) is much less evident.

During the interval of high flow intensity the effects of mesh refinement are more important than time step refinement. As the mesh is refined, time steps are larger as spurious oscillations are reduced (see Figure 7). Although it is apparent that very fine meshes are necessary to resolve all the features of the flow, the character of the flow is captured with all three meshes. As ε is reduced from 1×10^{-3} to 1×10^{-4} for the 48×18 mesh, Δt decreases by approximately a factor of two. This result is consistent with the scaling relationship $\Delta t \sim \varepsilon^{1/3}$ for the TR predictor–corrector method.[33] The decrease in ε results in very small changes in the curves for h_A and $v_{x,A}$. As a final measure of solution accuracy, the total mass in the system changed by 0·0023% over the course of the simulation for the 64×24 mesh with $\varepsilon = 1 \times 10^{-3}$.

4.4 Time-dependent results for $Gr = 1 \times 10^6$ and $Ma = 100$

Time-dependent results were obtained for $Gr = 1 \times 10^6$ and $Ma = 100$ with the other dimensionless groups given by equation (33). The initial condition is a steady state solution for the same trough containing a liquid metal with a viscosity larger by a factor of 10. The dimensionless groups for this solution are $Gr = 1 \times 10^4$, $Ma = 10$, $Ca = 1 \times 10^{-3}$, $St = 2{\cdot}5 \times 10^{-4}$ and $Pr = 0{\cdot}15$. The creeping flow solution for the previous case with $Gr = 1 \times 10^6$ and $Ma = 0$ is not used with the very strong surface Marangoni effect, which immediately accelerates the fluid near the free surface. In the presence of this surface effect it was felt that the flow could be developed more efficiently with an initial condition closer to the final condition. This contrasts with the previous case ($Ma = 0$) in which the flow is accelerated by a body force that is of the same scale across the flow domain.

In the simulations performed, the BE method was employed to varying degrees to improve the calculation efficiency during the flow development interval. From $t = 0$ to a time denoted by t_1, the BE method was used to damp localized oscillations associated with the initial shock and development of the thin momentum boundary layer at the free surface. For the balance of the simulation ($t > t_1$) the TR method was applied. In one simulation the 64×24 mesh was used with $t_1 = 1{\cdot}1$, while in three other calculations the 48×18 mesh was employed with $t_1 = 4 \times 10^{-5}$, 0·01 and 1·1. In all cases four BE steps of size 1×10^{-5} were initially taken.[34] The values for t_1 can be related to the time for

development of a flow boundary layer. A developed boundary layer has a characteristic thickness $\delta_s \sim (\nu h/v_s)^{1/2}$ and a development time δ_s^2/ν. Applying the variables of equation (6) gives unity as the characteristic boundary layer development time.

A sequence of streamlines and temperature contours is shown in Figure 8 for the 64×24 mesh and $t_1 = 1{\cdot}1$. The closely spaced streamlines near the free surface indicate a thin boundary layer and strong acceleration. At each time there are two primary cells with counterclockwise circulation. Although other smaller cells form and disappear, the basic appearance of the flow field remains unchanged. This result is attributed to the stabilizing influence of the Marangoni effect. The temperature contours reveal a thermal convection component of moderate strength.

The smooth streamlines and temperature contours suggest that the 64×24 mesh is sufficiently fine to resolve the flow and temperature fields. Also shown in Figure 8 are streamlines at $t = 6$ for the 48×18 mesh with $t_1 = 0{\cdot}01$ and $1{\cdot}1$. There are some indications of inadequate spatial resolution in the region between the two primary cells, but in general the streamlines are similar to those for the 64×24 mesh.

The variables Δt, h_A, and $v_{x,614A}$ are plotted versus time in Figure 9 for the four cases described above. A fourth variable $v_{y,614B}$ is also shown which is particularly sensitive to flow fluctuations near the downstream contact line (see Figure 2). There is a flow development period ($0 \leq t \leq 4$) in which values for Δt are generally larger than the later quasi-steady state values. During this development interval there is a jump in Δt for each curve at $t = t_1$ as the BE method is switched to the TR method. This jump size increases dramatically with t_1, but does not depend strongly on mesh size. During the flow development period, values for Δt are generally larger as t_1 is increased. It is apparent that extended use of the BE method can be of significant computational benefit. Although not done here, it is likely that a value of t_1 can be found that makes the best use of the damping properties of the BE method and the inherent efficiency of the TR method.

During the flow development period the flow intensity is relatively small and the changes in h_A and $v_{x,614A}$ are gradual (see Figure 9). The results for these variables do not depend strongly on mesh size or the value for t_1. After flow development, higher-frequency components appear in the curves for h_A and $v_{x,614A}$. For the 48×18 mesh with $t_1 = 0{\cdot}01$ and $1{\cdot}1$ the curves are similar until $t = 6$, at which point the differences grow. For the 64×24 mesh the fluctuations are smaller and less frequent,

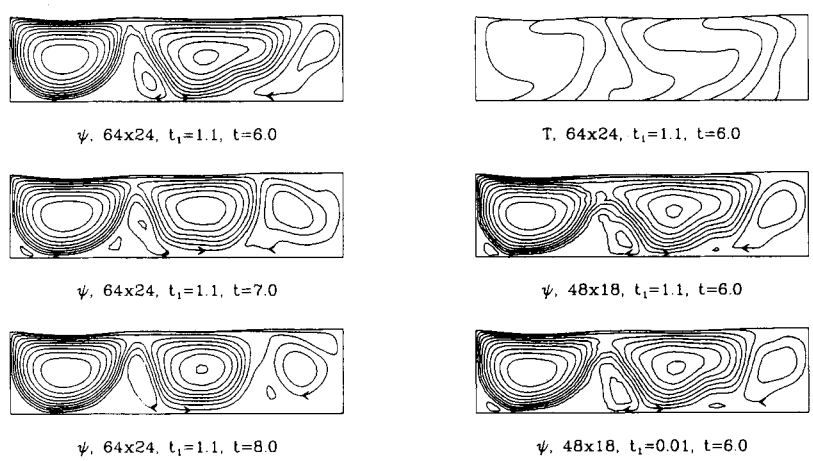

Figure 8. Time-dependent streamlines and temperature contours for $Gr = 1 \times 10^6$, $Ma = 100$, $Ca = 1 \times 10^{-4}$, $St = 2{\cdot}5 \times 10^{-5}$, $Pr = 0{\cdot}015$, 64×24 mesh and $\varepsilon = 1 \times 10^{-3}$. Twelve equal increments in ψ for $\psi_{min} \leq \psi \leq \psi_{max}$. Ten equal increments in T for $0 \leq T \leq 4$

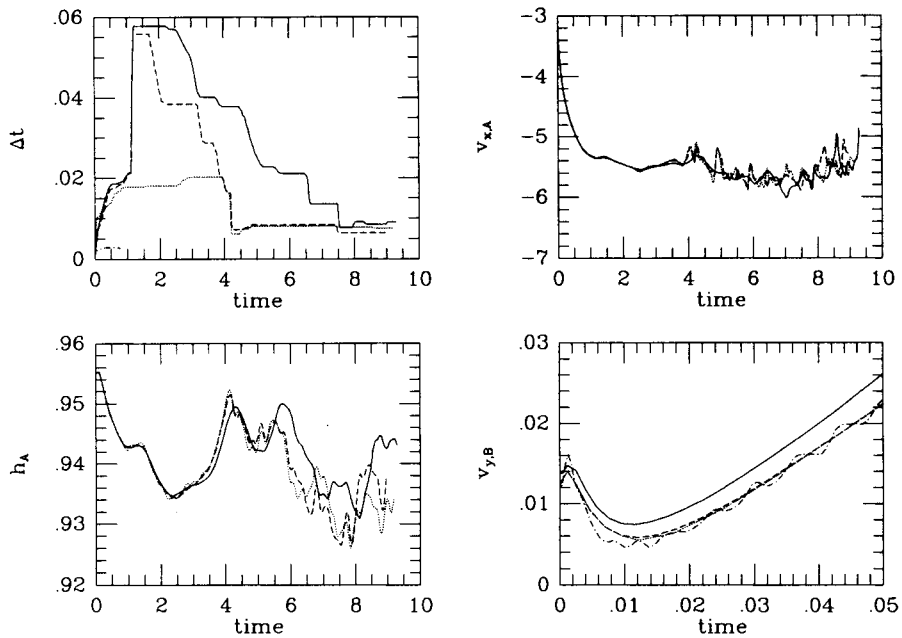

Figure 9. Time step size, pool depth and v_x at location A versus time for $Gr = 1 \times 10^6$, $Ma = 100$, $Ca = 1 \times 10^{-4}$, $St = 2{\cdot}5 \times 10^{-5}$ and $Pr = 0{\cdot}015$.————, 64 × 24, $t_1 = 1{\cdot}1$; — — —, 48 × 18, $t_1 = 1{\cdot}1$; · · · · ·, 48 × 18, $t_1 = 0{\cdot}01$; – · – · –, 48 × 18, $t_1 = 4 \times 10^{-5}$

indicating that some of those for the 48 × 18 mesh are spurious. None the less, the important low-frequency variations are captured fairly well in all cases.

The question arises as to why the extended use of the BE method during flow development provides such large improvements in numerical efficiency. The curves for h_A and $v_{x,615A}$ do not provide obvious clues since they are similar for all cases. An examination of curves for $v_{y,615B}$ provides some insight (see Figure 9). For $t_1 = 0{\cdot}01$ and $1{\cdot}1$, $v_{y,615B}$ increases monotonically after a small oscillation. In contrast, small-amplitude oscillations are observed for the case $t_1 = 4 \times 10^{-5}$. These localized oscillations are the result of the sudden change in flow conditions at the beginning of the calculation. It is evident that application of the BE method with $t_1 \geq 0{\cdot}01$ damps these oscillations. Noting the much larger values of Δt, it is apparent that extended use of the BE method during start-up can greatly improve numerical efficiency with a small loss in physical detail.

It is useful to compare these results with those for the previous set of simulations in which $Gr = 1 \times 10^6$ and $Ma = 0$. For both $Ma = 0$ and 100 there are generally two primary cells with strong circulation (see Figures 6 and 8). For $Ma = 100$ a thin boundary layer is formed by the strong shear force present at the free surface. Observing that the overall changes in the flow pattern are less pronounced for $Ma = 100$, it seems that the Marangoni effect stabilizes the flow despite the accompanying increase in flow intensity. This stabilization is also seen in the variable $v_{x,615A}$, which exhibits fluctuations of much smaller amplitude for $Ma = 100$ (see Figures 7 and 9).

5. CONCLUSIONS

The key results of this analysis are numerical solutions for time-dependent liquid metal flows with free convection, free surfaces and Marangoni effects. Flow intensities overlap the range corresponding to pool flows in electron beam vaporizers. The spatial discretization is accomplished using the Galerkin

finite element method and the time integration is performed using the backward Euler method and trapezoid rule with step size control. This approach provides for the completely implicit solution of the equations of change. The trapezoid rule is employed in the majority of situations, while the backward Euler method is used to damp localized oscillations associated with initial shocks and boundary layer development.

Flow intensities are large and rearrangements in the flow pattern are dramatic for the time-dependent flow driven by buoyancy forces alone ($Gr = 1 \times 10^6$, $Ma = 0$). For this case the effects of mesh refinement are much more important than time step refinement. The finest mesh appears to adequately resolve the flow, while the coarser meshes produce spurious oscillations but still capture the important features of the flow.

For the time-dependent case involving buoyancy and Marangoni forces ($Gr = 1 \times 10^6$, $Ma = 100$), the flow intensity is larger, but the rearrangements in flow pattern are less pronounced when compared with the case with $Ma = 0$. This apparent stabilization is attributed to the strong shear force present at the free surface. The effects of mesh refinement are significant, but the finest mesh seems to adequately resolve the flow. With some loss of detail, the extended initial use of the backward Euler method significantly improves the calculation efficiency.

ACKNOWLEDGEMENTS

The author expresses his appreciation to Bruce A. Finlayson for helpful discussions. The assistance of Pamela J. Meyer in performing the simulations and Kenneth W. Westerberg in reviewing the manuscript is also gratefully acknowledged. This work was performed under the auspices of the U.S. Department of Energy by Lawrence Livermore National Laboratory under Contract W-7405-Eng-48.

APPENDIX I: CALCULATION OF STREAMLINES

The streamfunction ψ is calculated as the solution to a Dirichlet problem

$$\frac{\partial^2 \psi}{\partial x^2} + \frac{\partial^2 \psi}{\partial y^2} = \frac{\partial v_y}{\partial x} - \frac{\partial v_x}{\partial y}, \tag{A36}$$

in which the boundary condition is obtained by evaluating the integral[47]

$$\psi = \psi_0 - \int_c (\mathbf{v} \cdot \mathbf{n})\, ds. \tag{A37}$$

Here v is the solution to the flow problem and ψ_0 is an arbitrary constant taken to vanish at the origin. In the finite element solution procedure the streamfunction and velocity components are represented by the biquadratic functions $\Phi^i(x, y)$.

APPENDIX II: NOMENCLATURE

BE	backward Euler method
f	dimensionless frequency
h	dimensionless depth of liquid in trough
k	thermal conductivity (ML/t^3T)
L	length of trough (L)
N	total number of nodes
N_h	total number of free surface nodes

N_p	total number of pressure nodes
n	outward-pointing unit vector for free surface
n_W	inward-pointing unit vector for trough
n_θ	outward-pointing unit vector for free surface at contact line
p	dimensionless isotropic pressure
q	dimensionless heat flux vector
R	dimensionless Galerkin residual
s	dimensionless distance measured along interface
s	unit vector tangent to surface
T	dimensionless temperature
TR	trapezoid rule
T_0, T_1	temperatures at $x=0$ and $x=4$ (T)
t	dimensionless time
t_1	dimensionless time at which BE method is switched to TR method
v	dimensionless velocity vector
v_s	characteristic velocity defined in equation (7) (L/t)
v_x, v_y	dimensionless x- and y-components of velocity vector
X	dimensionless position vector for liquid–gas interface
x	dimensionless position vector

Greek letters

α	thermal diffusivity (L^2/t)
β	thermal coefficient of volumetric expansion, $(-\partial \ln \rho/\partial T)_p$ (1/T)
Γ^j	bilinear polynomial for finite element method
$\boldsymbol{\delta}$	unit tensor
$\boldsymbol{\delta}_k$	unit vector in direction k
ε	error specification for time integration
θ_c	contact angle
μ	viscosity (M/Lt)
ν	momentum diffusivity (L^2/t)
$\boldsymbol{\pi}$	dimensionless total stress tensor defined in equation (4)
σ	surface tension (M/t^2)
$\boldsymbol{\tau}$	dimensionless viscous stress tensor, $-[\nabla v+(\nabla v)^\dagger]$
Φ^i	biquadratic polynomial for finite element method
ψ	dimensionless streamfunction

Superscripts

i	index for node
j	index for pressure node
k	index for surface node
+	dimensional quantity

Subscripts

A	location A; see Figure 2
B	location B; see Figure 2
m	quantity that moves with the mesh
s	standard or characteristic value
x, y	x- and y-directions
0	evaluated at wall $x=0$ or value for unstretched mesh
1	evaluated at wall $x=4$

REFERENCES

1. R. J. Hill (ed.), *Physical Vapor Deposition*, BOC Group Inc., 1986, pp. 17–110.
2. A. D. W. Jones, 'Hydrodynamics of Czochralski growth—a review of the effects of rotation and buoyancy forces', *Prog. Cryst. Growth Charact.*, **9**, 139–168 (1984).
3. W. E. Langlois, 'Buoyancy-driven flows in crystal-growth melts', *Ann. Rev. Fluid Mech.*, **17**, 191–215 (1985).
4. M. E. Glicksman, S. R. Coriell and G. B. McFadden, 'Interaction of flows with the crystal–melt interface', *Ann. Rev. Fluid Mech.*, **18**, 307–335 (1986).
5. R. A. Brown, 'Theory of transport processes in single crystal growth from the melt: a review', *AIChE J.*, **34**, 881–911 (1988).
6. G. Muller, D. T. J. Hurle and H. Wenzl (eds), 'Proc. First NATO Workshop on Computer Modeling in Crystal Growth from the Melt', *J. Cryst. Growth*, **97**, 1–243 (1989).
7. M. C. Tsai and S. Kou, 'Marangoni convection in weld pools with a free surface', *Int. j. numer. methods fluids*, **9**, 1503–1516 (1989).
8. T. Zacharia, S. A. David and J. M. Vitek, 'Effect of convection on weld pool development', in *The Metal Science of Joining: Proceedings of a Symposium*, TMS, Warrendale, PA, 1992.
9. R. T. Choo and J. Szekely, 'Vaporization kinetics and surface temperature in a mutually coupled spot gas tungsten arc weld and weld pool', *Weld. Res.*, **71**, 77s–93s (1992).
10. S. Mishima and J. Szekely, 'The modeling of fluid flow and heat transfer in mold filling', *ISIJ Int.*, **29**, 324–332 (1989).
11. G. Dhatt, D. M. Gao and A. Ben Cheikh, 'A finite element simulation of metal flow in moulds', *Int. j. numer. methods eng.*, **30**, 821–831 (1990).
12. R. Song, G. Dhatt and A. Ben Cheikh, 'Thermo-mechanical finite element model of casting systems', *Int. j. numer. methods eng.*, **30**, 579–599 (1990).
13. H. S. Kheshgi and P. M. Gresho, 'Analysis of electron-beam vaporization of refractory metals', in *Electron Beam: State of the Art 1986*, 1986, pp. 68–79.
14. I. P. Jones, 'Low Prandtl free convection in a vertical slot', *AERE Harwell Report R-10416*, 1981–1982.
15. C. Benocci, 'Thermohydraulics of liquid metals: turbulence modeling in liquid metal free convection', *Von Karman Institute Lecture Series 1983–07*, 1983.
16. P. M. Gresho and C. G. Upson, 'Application of a modified finite element method to the time-dependent thermal convection of a liquid metal', in C. Taylor, C. Johnson, J. A. Smith and W. Ramsey (eds), *Proc. 3rd Int. Conf. on Numerical Methods in Laminar and Turbulent Flow*, Pineridge, Swansea, 1983, pp. 750–762.
17. A. A. Mohamad and R. Viskanta, 'Transient natural convection of low-Prandtl-number fluids in a differentially heated cavity', *Int. j. numer. methods fluids*, **13**, 61–81 (1991).
18. M. Mihelcic, K. Wingerath and Chr. Pirron, 'Three-dimensional simulations of the Czochralski bulk flow', *J. Cryst. Growth*, **69**, 473–488 (1984).
19. M. Mihelcic and K. Wingerath, 'Instability of buoyancy driven convection in Si melts during Czochralski crystal growth', *J. Cryst. Growth*, **97**, 42–49 (1989).
20. G. Muller, G. Neumann and H. Matz, 'A two-Rayleigh-number model of buoyancy-driven convection in vertical melt growth configurations', *J. Cryst. Growth*, **84**, 36–49 (1987).
21. J. Baumgartl, W. Budweiser, G. Muller and G. Neumann, 'Studies of buoyancy driven convection in a vertical cylinder with parabolic temperature profile', *J. Cryst. Growth*, **97**, 9–17 (1989).
22. A. Bottaro and A. Zebib, 'Three-dimensional thermal convection in Czochralski melt', *J. Cryst. Growth*, **89**, 50–58 (1989).
23. M. J. Crochet, F. T. Geyling and J. J. Van Schaftingen, 'Numerical simulation of the horizontal Bridgman growth of a gallium arsenide crystal', *J. Cryst. Growth*, **65**, 166–172 (1983).
24. M. J. Crochet, F. T. Geyling and J. J. Van Schaftingen, 'Numerical simulation of the horizontal Bridgman growth. Part I: Two-dimensional flow', *Int. j. numer. methods fluids*, **7**, 29–47 (1987).
25. K. H. Winters, 'Oscillatory convection in crystal melts: the horizontal Bridgman process', *Proc. 5th Int. Conf on Numerical Methods in Thermal Problems*, Pineridge, Swansea, 1987, pp. 299–310.
26. B. Roux, G. de Vahl Davis, M. Deville, R. L. Sani and K. H. Winters, 'General synthesis of the results', in B. Roux (ed.), *Numerical Simulation of Oscillatory Convection in low Pr-Fluids*, Vieweg, Braunschweig, 1990, pp. 285–304.
27. B. Roux and H. Ben Hadid, 'Numerical simulation of oscillatory convection in semiconductor melts', *J. Cryst. Growth*, **97**, 201–216 (1989).
28. R. A. Brown, T. A. Kinney, P. A. Sackinger and D. E. Bornside, 'Toward an integrated analysis of Czochralski growth', *J. Cryst. Growth*, **97**, 99–115 (1989).
29. P. A. Sackinger, R. A. Brown and J. J. Derby, 'A finite element method for analysis of fluid flow, heat transfer, and free interfaces in Czochralski crystal growth', *Int. j. numer. methods fluids*, **9**, 453–492 (1989).
30. H. Ben Hadid and B. Roux, 'Buoyancy- and thermocapillary-driven flows in a shallow open cavity: unsteady flow regimes', *J. Cryst. Growth*, **97**, 217–225 (1989).
31. D. Villers and J. K. Platten, 'Influence of thermocapillarity on the oscillatory convection in low-*Pr* fluids', in B. Roux (ed.), *Numerical Simulation of Oscillatory Convection in Low-Pr Fluids*, Vieweg, Braunschweig, 1990, pp. 108–116.
32. S. F. Kistler and L. E. Scriven, 'Coating flows', in J. R. A. Pearson and S. M. Richardson (eds), *Computational Analysis of Polymer Processing*, Applied Science, London, 1983, pp. 243–299.
33. P. M. Gresho, R. L. Lee and R. L. Sani, 'On the time-dependent solution of the incompressible Navier–Stokes equations in two and three dimensions', in *Recent Advances in Numerical Methods in Fluids*, Vol. 1, Pineridge, Swansea,

1980, pp. 27–79.
34. H. S. Kheshgi and L. E. Scriven, 'Penalty finite element analysis of unsteady free surface flows', in R. H. Gallagher (ed.), *Finite Elements in Fluids*, Vol. 5, Wiley, Chichester, 1984, pp. 393–434.
35. J. J. Derby, L. J. Atherton, P. D. Thomas and R. A. Brown, 'Finite element methods for analysis of the dynamics and control of Czochralski crystal growth', *J. Sci. Comput.*, **2**, 297–343 (1987).
36. B. A. Finlayson, *Numerical Methods for Problems with Moving Fronts*, Ravenna Park, 1993, pp. 299–300.
37. L. E. Scriven, 'Dynamics of a fluid interface. Equation of motion for Newtonian surface fluids', *Chem. Eng. Sci.*, **12**, 98–108 (1960).
38. S. Dupont, J. M. Marchal and M. J. Crochet, 'Numerical simulation of the horizontal Bridgman growth. Part II: Three-dimensional flow', *Int. J. Numer. Methods Fluids*, **7**, 49–67 (1987).
39. K. J. Ruschak, 'A method for incorporating free boundaries with surface tension in finite element fluid-flow simulators', *Int. j. numer. methods fluids*, **15**, 639–648 (1980).
40. S. L. Josse and B. A. Finlayson, 'Reflections on the numerical viscoelastic flow problem', *J. Non-Newtonian Fluid Mech.*, **16**, 13–36 (1984).
41. P. Hood, 'Frontal solution program for unsymmetric matrices', *Int. j. numer. methods eng.*, **10**, 379–399 (1976).
42. L. Gourmiri and J. C. Joud, 'Auger electron spectroscopy study of aluminium–tin liquid system', *Acta Metall.*, **30**, 1397–1405 (1982).
43. M. Behnia and G. de Vahl Davis, 'Fine mesh solutions using stream function–vorticity formulation', in B. Roux (ed.), *Numerical Simulation of Oscillatory Convection in Low-Pr Fluids*, Vieweg, Braunschweig, 1990, pp. 11–18.
44. M. A. McClelland, 'Time-dependent free convection of liquid metals. Part I: Flow in a rigid cavity', *Lawrence Livermore National Laboratory, UCRL-JC-110097 Pt 1*, 1992.
45. M. A. McClelland, 'Time-dependent free convection of liquid metals. Part II: Flow with a deformable interface', *Lawrence Livermore National Laboratory, UCRL-JC-110097 Pt 2*, 1992.
46. H. Lamb, *Hydrodynamics*, Dover, New York, 1932, pp. 440–442.
47. B. A. Finlayson, 'Stream functions derived from velocity fields', personal communication, 1981.